



OPEN

Facile synthesis of FeCeO_x nanoparticles encapsulated carbon nitride catalyst for highly efficient and recyclable synthesis of substituted imidazoles

Najmedin Azizi[✉], Mostafa Saadat & Mahtab Edrisi

Herein, we developed a novel composite called $\text{FeCeO}_x@g\text{-C}_3\text{N}_4$ through a combination of sonication, sintering, and hydrothermal techniques to implement the principles of green chemistry by utilizing reusable nanocomposites in one-pot reactions. To gain a comprehensive understanding of the catalyst's structure, composition, and morphology, various characterization methods were employed. These included FT-IR analysis to examine chemical bonds, SEM and TEM imaging to visualize the catalyst's surface and internal structure, TGA to assess thermal stability, EDS for elemental composition analysis, and XRD to determine crystal structure. The $\text{FeCeO}_x@g\text{-C}_3\text{N}_4$ nanocatalyst demonstrated remarkable efficacy in the one-pot synthesis of 2,4,5-trisubstituted and 1,2,4,5-tetrasubstituted imidazole. Noteworthy features of this catalyst included high percentage yield, mild reaction conditions, short reaction time, and an efficient and straightforward procedure. Furthermore, the $\text{FeCeO}_x@g\text{-C}_3\text{N}_4$ composite exhibited excellent recyclability and reusability. It could be recycled and reused up to four times without a significant decline in catalytic activity.

Imidazole derivatives have gained significant importance due to their biological activity in natural products, biology, intermediates, and pharmacologically active compounds¹. The presence of a lone pair of nitrogen in the imidazole ring enables the formation of hydrogen bonding, which contributes to their metal-binding capability. This property has found applications in the pharmaceutical industry^{2–5}. In recent years, imidazole compounds have garnered widespread attention due to their diverse range of properties and applications. These compounds exhibit antibiotic, anti-tumoral, pesticide, herbicide, anti-allergy, anti-viral, and other pharmacological activities^{6,7}. Moreover, the imidazole structure is present in various drugs such as losartan, eprosartan, histidine, and histamine⁸.

Two important imidazole derivatives are 1,2,4,5-tetraphenylimidazole and 2,4,5-triphenylimidazole. The first imidazole compound was reported by Radziszewski, Japp, and Robinson in 1882. They achieved its synthesis by reacting 1,2-dialdehyde with ammonium chloride. Since then, several imidazoles have been reported, derived from 1,2-diketones, α -ketomonoximes, α -hydroxy ketones in combination with aldehydes and ammonium^{9,10}. These imidazole derivatives have found numerous applications and gained importance across various industries¹¹. Considering the significant applications of imidazole derivatives, several synthetic protocols with high yield and efficiency have been documented in the literature¹². However, some of these protocols utilize toxic and expensive catalysts that are less efficient. Consequently, they often involve harsh reaction conditions, long reaction times, and yield limitations^{13–15}.

Graphitic carbon nitride ($g\text{-C}_3\text{N}_4$) has garnered significant attention and found applications in various energy-related fields¹⁶. $g\text{-C}_3\text{N}_4$ primarily consists of carbon and nitrogen atoms and possesses desirable properties such as easy synthesis and functionalization, excellent physicochemical stability, wide bandgap, low toxicity, and cost-effectiveness. The unique properties of $g\text{-C}_3\text{N}_4$, such as its functionalization capabilities, physicochemical stability, and low cost, make it an attractive choice for supporting other catalysts or functional materials^{17–21}. One key advantage of $g\text{-C}_3\text{N}_4$ is its covalent bond nature, which results in an inactive surface that reduces the interaction between hydrogen and oxygen^{22–24}. This characteristic enhances its catalytic properties^{19,25,26}. However, pure

Chemistry and Chemical Engineering Research Center of Iran, P.O. Box 14335-186, Tehran, Iran. ✉email: azizi@ccerci.ac.ir

g-C₃N₄ has two main limitations: first, it absorbs only a small fraction of solar energy, primarily in the range of low bandgap wavelengths (below 460 nm). Second, the fast recombination of double electrons within the cavities of g-C₃N₄ leads to a decrease in photocatalytic activity^{27–30}. To address these limitations, various approaches have been developed to enhance the catalytic activity of g-C₃N₄ and mitigate imperfections³¹. These approaches include doping g-C₃N₄ with transition metals^{32–35} and coupling it with metals^{36–41}. These strategies aim to improve the absorption of a broader range of solar energy, reduce electron recombination, and enable the recovery and recycling of g-C₃N₄, thereby enhancing its overall performance as a catalyst^{42–44}.

Magnetic materials offer a range of advantages due to their inherent magnetism and unique properties^{45,46}. They are crucial in various industries and applications⁴⁷. Magnetic storage devices rely on their ability to retain magnetization, enabling high-capacity data storage⁴⁸. Electric motors and generators utilize magnetic materials for efficient energy conversion⁴⁹. Magnetic sensors enable precise detection and measurement of magnetic fields in compasses, position sensing, and current sensing⁵⁰. In industries like mining and recycling, magnetic materials facilitate effective separation techniques⁵¹. Biomedical applications benefit from magnetic nanoparticles in imaging, drug delivery, and cancer treatment⁵². Magnetic materials also play a vital role in non-destructive testing and offer versatility for customization⁵³.

In our continue interest to the expanding knowledge of carbon nitride-based catalysts and their application in various organic transformations^{54–56}, herein, we successfully prepared FeCeO_x@g-C₃N₄ nanocomposites, which serve as a novel catalyst with excellent activity in the one-pot synthesis of 1,2,4,5-tetraphenylimidazole and 2,4,5-triphenylimidazole derivatives under mild reaction conditions. By combining FeCeO_x with g-C₃N₄, we have fabricated a catalyst with enhanced performance and activity that offer practical benefits, such as energy efficiency and environmental friendliness.

Results and discussion

Catalyst characterization

SEM

The morphology and microstructure of the FeCeO_x@g-C₃N₄ nanocomposite were investigated using SEM analysis. The obtained SEM images of FeCeO_x@g-C₃N₄ clearly demonstrate the deposition of FeCeO_x on the surface of g-C₃N₄, as shown in Fig. 1. The SEM images reveal a 2D sheet-like network structure with a uniform distribution of Fe and Ce species on the surface of g-C₃N₄. This indicates successful incorporation of FeCeO_x onto the g-C₃N₄ framework. Importantly, the absence of aggregated species suggests good dispersion and adherence of FeCeO_x nanoparticles on the g-C₃N₄ surface.

EDS

The chemical composition of FeCeO_x@g-C₃N₄ was further confirmed through EDS spectrum analysis. The EDS spectrum, as shown in Fig. 2, reveals the presence of elements associated with Ce, Fe, O, N, and C. The appearance of these elements in the EDS spectrum provides strong evidence for the incorporation of Ce and Fe in the nanocomposite. The presence of Ce indicates the successful integration of CeO_x, while Fe confirms the presence of FeO_x. This supports the earlier observations from SEM analysis, indicating the successful deposition of FeCeO_x nanoparticles onto the g-C₃N₄ framework.

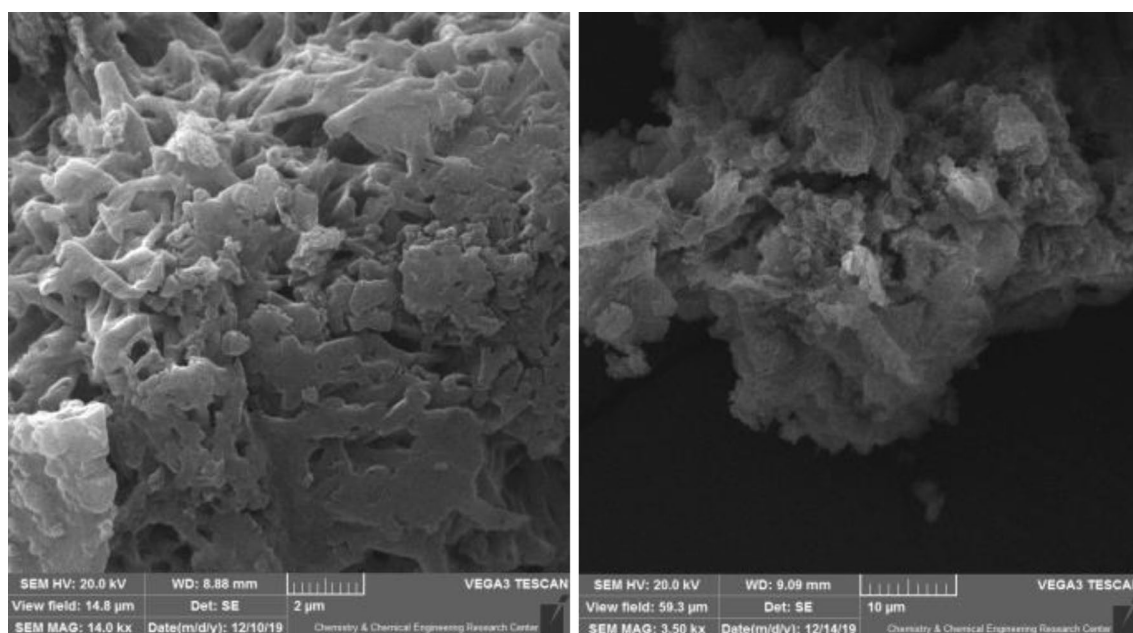


Figure 1. SEM images of FeCeO_x@g-C₃N₄ nanocomposite.

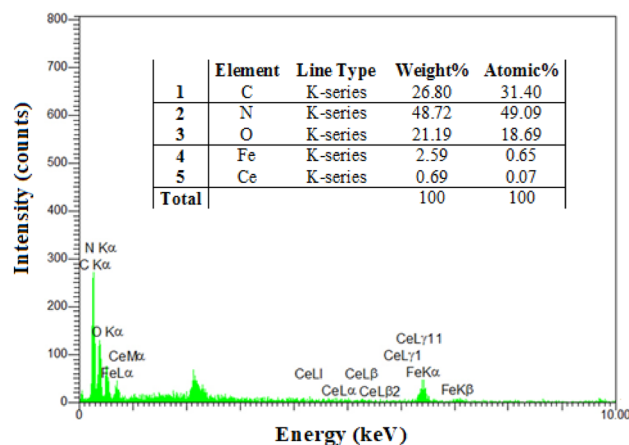


Figure 2. The EDS analysis of $\text{FeCeO}_x@g\text{-C}_3\text{N}_4$ nanocomposite.

XRD

The crystal structure of the composite was characterized using a powder X-ray diffractometer (XRD). As shown in Fig. 3, five reflections are observed in the XRD pattern of Fe_2O_3 26.9°, 35.42°, 43.3°, 56.1° and 61.3° that belong to the (2 2 0), (3 1 1), (4 0 0), (5 1 1) and (4 4 0) plane diffractions of Fe_2O_3 . In addition to the observed reflection at (3 1 1), (2 2 0), (2 0 0), and (1 1 1) belongs to CeO_2 . According to the typical characteristic diffraction peaks of $g\text{-C}_3\text{N}_4$, two characteristic diffraction peaks can be found at 13.1° and 27.4°.

FT-IR

FT-IR spectroscopy was employed to investigate the bonding states of the $\text{FeCeO}_x@g\text{-C}_3\text{N}_4$ nanocomposite. The FT-IR analysis confirms the presence of FeCeO_x on $g\text{-C}_3\text{N}_4$. In Fig. 4, several absorption bands are observed, each corresponding to specific bonding vibrations. The strong absorption band at 580 cm^{-1} is attributed to the Fe–O stretching mode, providing evidence for the presence of FeO in the nanocomposite. Additionally, the absorption bands at 740 cm^{-1} and 1416 cm^{-1} are assigned to the Ce–O stretching vibrations, further confirming the presence of CeO_2 . The absorption band at 804 cm^{-1} corresponds to the bending vibration of the s-triazine ring in $g\text{-C}_3\text{N}_4$, indicating the presence of $g\text{-C}_3\text{N}_4$ in the nanocomposite. The absorption bands in the range of $1200\text{--}1400\text{ cm}^{-1}$ are attributed to the C–N stretching vibration mode present in $g\text{-C}_3\text{N}_4$. Furthermore, the absorption band at 1637 cm^{-1} corresponds to the C=N stretching vibration mode, providing further evidence of the presence of $g\text{-C}_3\text{N}_4$ in the nanocomposite. The broad absorption band observed in the range of $2800\text{--}3500\text{ cm}^{-1}$ is indicative of the N–H stretching vibrations of amine groups in $g\text{-C}_3\text{N}_4$ and the O–H stretching vibrations of absorbed water from the environment.

The detailed morphology and structure of the nanocomposite at the nanoscale level were showed in the TEM image of the $\text{FeCeO}_x@g\text{-C}_3\text{N}_4$ nanocomposite (Fig. 5). The image reveal FeCeO_x particles had good dispersity and uniform distribution of particle size on the surface of the $g\text{-C}_3\text{N}_4$ matrix. The $g\text{-C}_3\text{N}_4$ matrix, on the other hand, would appear as a continuous network of interconnected sheets or layers, forming a 2D structure. The

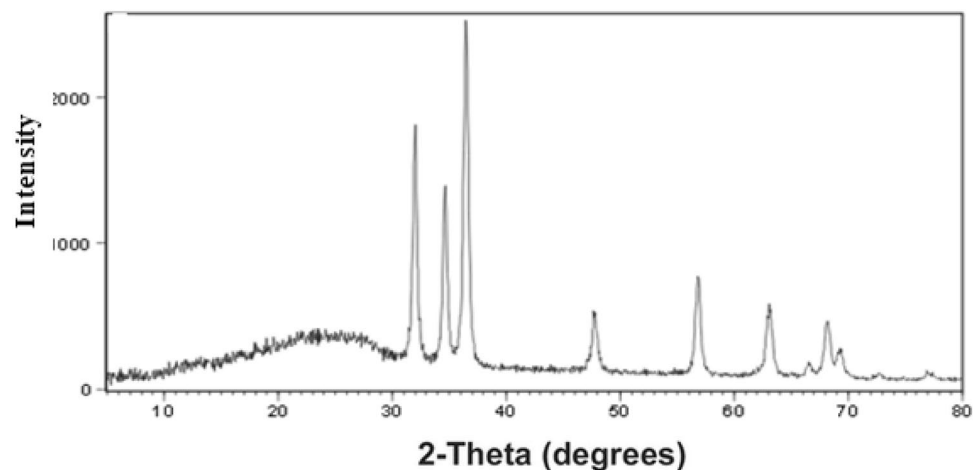


Figure 3. XRD spectra of $\text{FeCeO}_x@g\text{-C}_3\text{N}_4$ nanocomposite.

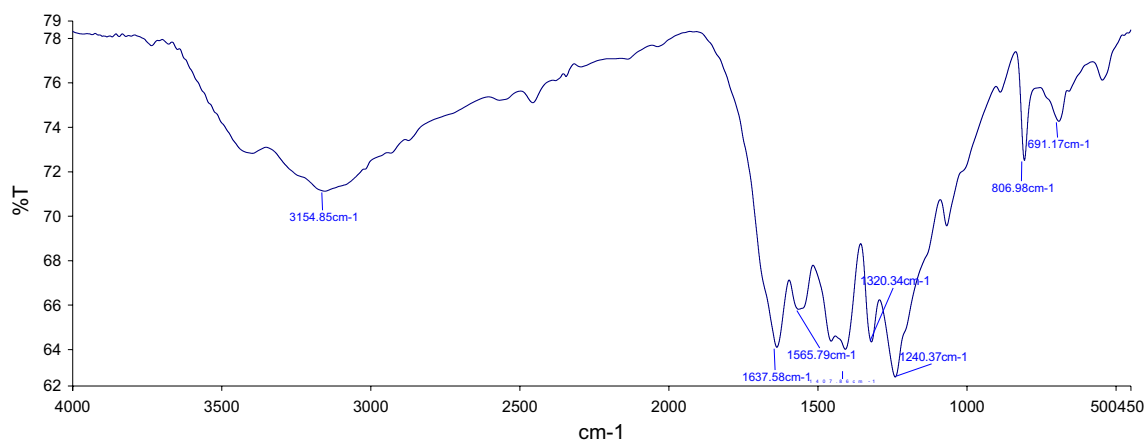


Figure 4. The FT-IR spectra of FeCeO_x@g-C₃N₄ nanocomposite.

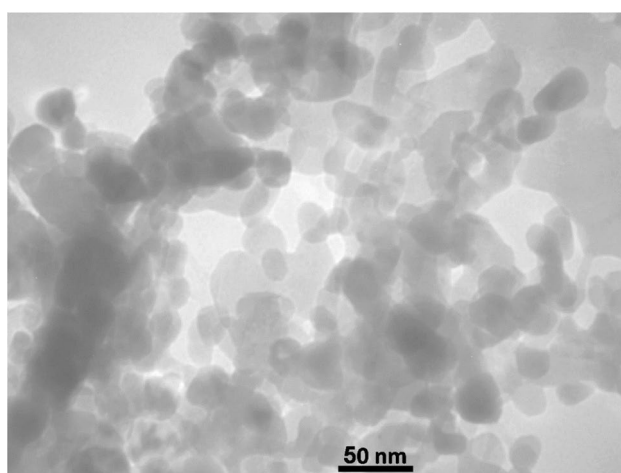


Figure 5. The TEM image of FeCeO_x@g-C₃N₄ nanocomposite.

g-C₃N₄ layers might exhibit a darker contrast compared to the nanoparticles, providing a contrasting background in the TEM image.

Measurement of the surface area of cavities in porous materials is important. Therefore, for the synthesized FeCeO_x@g-C₃N₄ nanocomposite, the surface area, pore volumes and pore size was measured and the obtained data are depicted in Table 1 and supporting information. Specific surface area of pure g-C₃N₄ is 41.14 m² g⁻¹. The specific surface area of the FeCeO_x/g-C₃N₄ sample, calculated using the BET equation, is 36.12 m² g⁻¹, which is lower compared to that of bare g-C₃N₄. The decrease of specific surface area along with lower pore volume indicates FeCeO_x is loaded to g-C₃N₄.

Thermogravimetric analysis (TGA) is a technique used to study the thermal behavior of a material as a function of temperature. It involves measuring the weight changes of a sample as it is heated or cooled under controlled conditions (Fig. 6). The TGA of the FeCeO_x@g-C₃N₄ revealed three stages of weight loss. The initial weight loss at lower temperatures due to the removal of surface-adsorbed species. These adsorbed species can include moisture, gases, or functional groups like OH groups that may be present on the composite surface. The major weight loss occurred between approximately 520–630 °C, which was attributed to the combustion of the graphitic carbon nitride phase.

| Sample | Surface area (m ² g ⁻¹) | Pore vol. (cm ³ g ⁻¹) | Pore radius (nm) |
|---|--|--|------------------|
| g-C ₃ N ₄ | 41.14 | 0.189 | 18.4 |
| FeCeO _x @g-C ₃ N ₄ | 36.12 | 0.147 | 12.9 |

Table 1. BET analysis summary of pure g-C₃N₄ and FeCeO_x@g-C₃N₄.

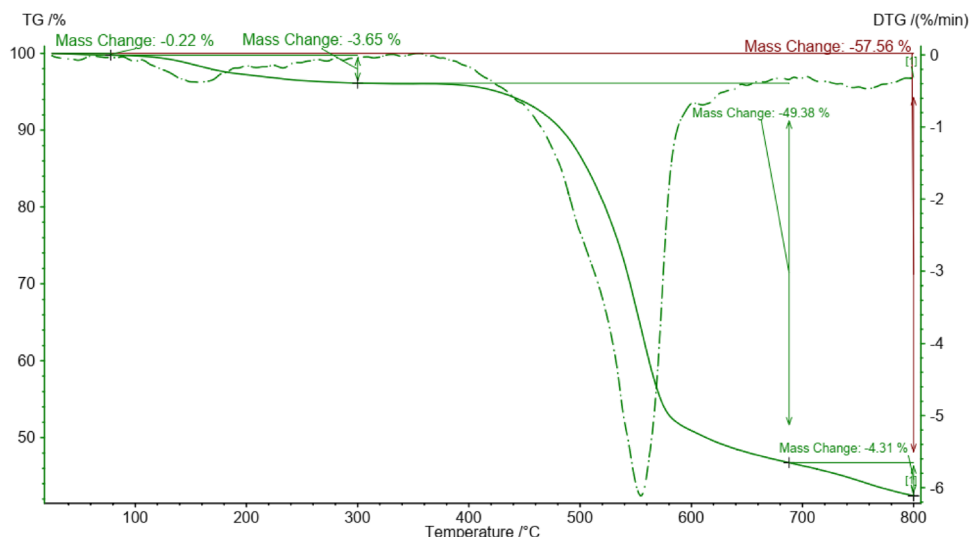


Figure 6. The TGA cure of $\text{FeCeO}_x\text{@g-C}_3\text{N}_4$ nanocomposite.

To validate the applicability of ICP-MS as alternatives to EDX analysis for the measurement of Ce in the composite, $\text{FeCeO}_x\text{@g-C}_3\text{N}_4$ nanocomposite were analyzed by ICP-MS. The amount of analyzed Ce (0.71 wt.%) corresponded to Ce content (0.69 wt.%) based on EDX measurement.

Assessment of catalytic activity of $\text{FeCeO}_x\text{@g-C}_3\text{N}_4$ nanocomposite for the synthesis of 2,4,5-trisubstituted and 1,2,4,5-tetrasubstituted imidazoles

After preparing and characterizing $\text{FeCeO}_x\text{@g-C}_3\text{N}_4$, the catalytic performance of the composites was investigated for the synthesis of 1,2,4,5-tetra phenyl imidazole and 2,4,5-triphenyl imidazole. This study aimed to develop a cost-effective and easily accessible method for synthesizing these imidazole derivatives using readily available starting materials. The catalytic protocol demonstrated excellent selectivity and simplicity, allowing for the synthesis of various 2,4,5-trisubstituted and 1,2,4,5-tetrasubstituted imidazoles. The procedure presented a sustainable and chemically efficient alternative, as it utilized inexpensive and readily available starting materials.

Optimization of the reaction parameters for the synthesis of 1,2,4,5-tetrasubstituted imidazoles

In the optimization study, benzaldehyde, benzil, aniline, and NH_4OAc were chosen as model substrates to prepare 1,2,4,5-tetrasubstituted imidazole. The goal was to identify the optimal reaction conditions by varying catalysts, solvents, and temperatures. Table 2 presents the results of the model reactions under different conditions. Entry 1 shows that the model reaction without a catalyst resulted in a low yield, indicating the importance of a catalyst in the reaction. Subsequently, various catalysts were tested in the model reaction (entries 2–6 and 8), and the best outcome was obtained with $\text{FeCeO}_x\text{@g-C}_3\text{N}_4$ as the catalyst (entry 8). Further investigation was conducted to determine the optimal catalyst amount (entries 7–10). The results in Table 2 revealed that using 20 mg of $\text{FeCeO}_x\text{@g-C}_3\text{N}_4$ as the catalyst (entry 8) provided the highest yield for synthesizing 1,2,4,5-tetraphenyl imidazoles using benzaldehyde (0.5 mmol), benzil (0.5 mmol), aniline (0.5 mmol), and ammonium acetate (0.5 mmol).

The optimization study further investigated the effect of temperature and solvent on the synthesis of 1,2,4,5-tetrasubstituted imidazole. Table 2 provided insights into the optimal reaction conditions. Regarding temperature, the results in Table 2 (entries 8 and 11) indicated that 60 °C was the best operating temperature for the model reaction, resulting in the highest yield of the desired product (Table 2, entry 8). Moreover, the impact of different solvents on the model reaction was explored (Table 2, entries 12–19). Among the solvents tested, ethanol (EtOH) was found to be the most suitable choice for this reaction, providing favorable yields of the 1,2,4,5-tetraphenylimidazole product. Based on the results presented in Table 2, the optimized conditions for the synthesis of 1,2,4,5-tetraphenylimidazole are as follows: benzaldehyde (0.5 mmol), benzil (0.5 mmol), aniline (0.5 mmol), and ammonium acetate (0.5 mmol) as the substrates, 20 mg of $\text{FeCeO}_x\text{@g-C}_3\text{N}_4$ nanocomposite as the catalyst, ethanol as the solvent, and a reaction temperature of 60 °C.

The relationship between reaction time and percent yield in the model reaction was evaluated by collecting experimental data points at various reaction times. These data points were then used to plot a graph, typically referred to as Fig. 7, to visualize the trend. According to the graph, it can be observed that there is an initial increase in the percent yield as the reaction progresses. This indicates that the desired product is being formed over time, leading to an improvement in yield. However, after reaching a certain point, the graph shows a plateau, where the percent yield remains relatively constant. Beyond the plateau, a continuous increase in the yields is observed. The continuous increase in yields indicates that the reaction is proceeding in a favorable direction, leading to higher overall conversion and yield.

After optimizing the reaction conditions for synthesizing 1,2,4,5-tetraphenyl imidazole, various benzaldehydes were utilized to prepare different imidazoles. The results of these reactions are presented in Table 3,

TON = 9.4×10^{-6} and TOF $1.3 \times 10^{-9} \text{ s}^{-1}$

| Entry | Catalysts | Catalyst (mg mol) | | time (min) | Solvent | Temp. (°C) | Yield (%) ^a |
|-------|---|-------------------|---------|------------|------------------|------------|------------------------|
| 1 | Without catalyst | – | – | 250 | Ethanol | 60 | 13 |
| 2 | g-C ₃ N ₄ | 20 | 0.022 | 150 | Ethanol | 60 | 28 |
| 3 | SbCl ₃ /g-C ₃ N ₄ | 20 | 0.00625 | 150 | Ethanol | 60 | 39 |
| 4 | FeCl ₃ /g-C ₃ N ₄ | 20 | 0.0078 | 150 | Ethanol | 60 | 71 |
| 5 | CeCl ₃ /g-C ₃ N ₄ | 20 | 0.0059 | 150 | Ethanol | 60 | 48 |
| 6 | FeCl ₃ /CeCl ₃ @g-C ₃ N ₄ | 20 | 0.0039 | 150 | Ethanol | 60 | 84 |
| 7 | FeCeO _x @g-C ₃ N ₄ | 10 | 0.0023 | 140 | Ethanol | 60 | 69 |
| 8 | FeCeO _x @g-C ₃ N ₄ | 20 | 0.0047 | 120 | Ethanol | 60 | 98 |
| 9 | FeCeO _x @g-C ₃ N ₄ | 35 | 0.007 | 120 | Ethanol | 60 | 98 |
| 10 | FeCeO _x @g-C ₃ N ₄ | 50 | 0.0115 | 120 | Ethanol | 60 | 98 |
| 11 | FeCeO _x @g-C ₃ N ₄ | 20 | 0.0047 | 120 | Ethanol | 25 | 82 |
| 12 | FeCeO _x @g-C ₃ N ₄ | 20 | 0.0047 | 120 | Water | 25 | 78 |
| 13 | FeCeO _x @g-C ₃ N ₄ | 20 | 0.0047 | 120 | Water | 60 | 83 |
| 14 | FeCeO _x @g-C ₃ N ₄ | 20 | 0.0047 | 120 | Methanol | 25 | 81 |
| 15 | FeCeO _x @g-C ₃ N ₄ | 20 | 0.0047 | 120 | Methanol | 60 | 88 |
| 16 | FeCeO _x @g-C ₃ N ₄ | 20 | 0.0047 | 120 | Acetonitrile | 60 | 79 |
| 17 | FeCeO _x @g-C ₃ N ₄ | 20 | 0.0047 | 120 | CCl ₄ | 60 | 82 |
| 18 | FeCeO _x @g-C ₃ N ₄ | 20 | 0.0047 | 120 | Ethyl acetate | 60 | 81 |
| 19 | FeCeO _x @g-C ₃ N ₄ | 20 | 0.0047 | 120 | DMF | 60 | 73 |
| 20 | CeO ₂ @g-C ₃ N ₄ | 20 | 0.0075 | 120 | Ethanol | 60 | 84 |
| 21 | Fe ₂ O ₃ @g-C ₃ N ₄ | 20 | 0.0079 | 120 | Ethanol | 60 | 48 |

Table 2. The effect of various parameters on the synthesis of 1,2,4,5-tetraphenyl imidazole. ^a Isolated yields.

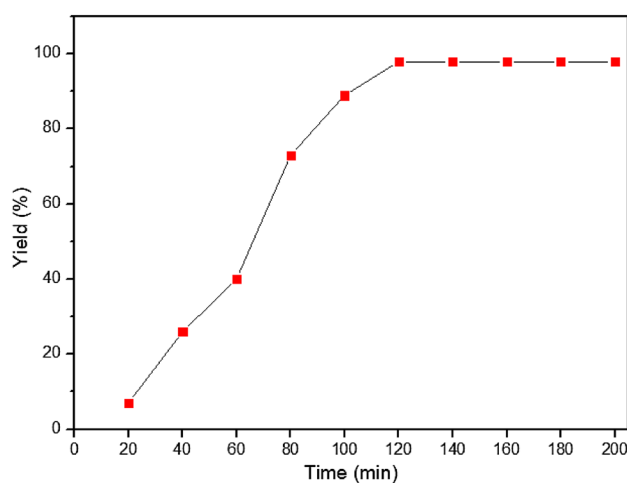
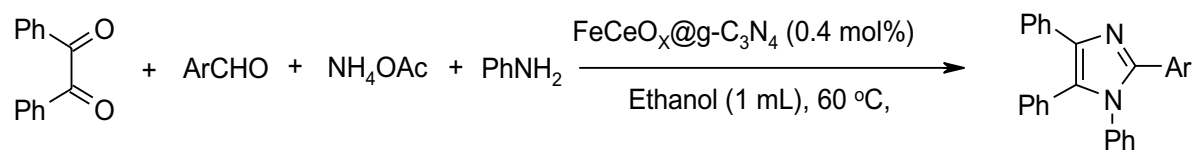


Figure 7. A graph of reaction time and yield on the model reaction.

shedding light on the influence of different substituents on the benzaldehyde. The Table 3 demonstrates that both electron-withdrawing and electron-rich groups on the benzaldehyde perform well in the reaction, leading to the formation of the corresponding 1,2,4,5-tetraphenyl imidazoles in excellent yields. This suggests that a wide range of benzaldehyde derivatives can be utilized as substrates in this transformation. However, when the benzaldehyde contains an electron-donating group substituent (Table 3, entry 4), the yield of the desired product decreases. On the other hand, if the benzaldehyde possesses a strong electron-withdrawing substituent (Table 3, entry 7), the yield increases. These observations indicate that the nature of the substituents on the benzaldehyde has a significant impact on the reaction outcome. Electron-withdrawing groups tend to enhance the reactivity



| Entry | Aldehyde | Product | Time (min) | Yield (%) ^a | Melting point | |
|-------|----------|---------|------------|------------------------|---------------|-----------------------|
| | | | | | Found | Reported |
| 1 | | | 120 | 98 | 219–220 | 218–219 ⁷ |
| 2 | | | 130 | 97 | 160–162 | 159–160 ² |
| 3 | | | 130 | 89 | 185–186 | 184–186 ² |
| 4 | | | 120 | 92 | 166–168 | 164–166 ⁹ |
| 5 | | | 120 | 81 | 281–283 | 285–286 ² |
| 6 | | | 120 | 95 | 156–158 | 154–156 ¹⁰ |

Continued

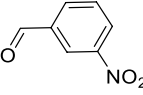
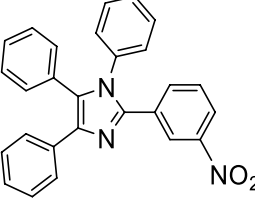
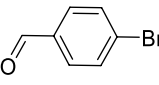
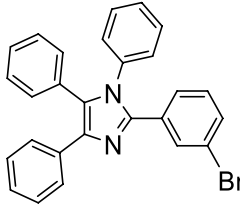
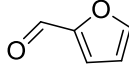
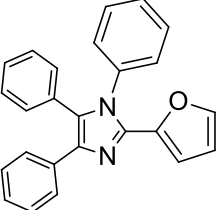
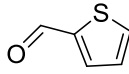
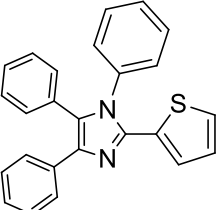
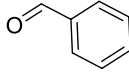
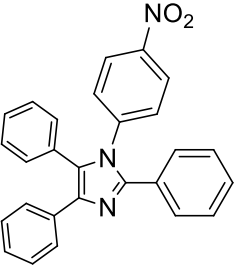
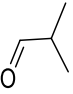
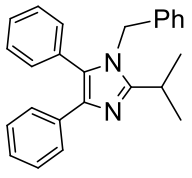
| $\text{Ph-C(=O)-C(=O)-Ph} + \text{ArCHO} + \text{NH}_4\text{OAc} + \text{PhNH}_2 \xrightarrow[\text{Ethanol (1 mL), 60 }^\circ\text{C,}]{\text{FeCeO}_x\text{/g-C}_3\text{N}_4 \text{ (0.4 mol\%)}}$ $\text{Ph-C}_2\text{N}_2\text{-C(Ar)-N(Ph)-C}_2\text{Ph}$ | | | | | | |
|--|---|---|------------|------------------------|---------------|-----------------------|
| Entry | Aldehyde | Product | Time (min) | Yield (%) ^a | Melting point | |
| | | | | | Found | Reported |
| 7 |  |  | 135 | 95 | 153–155 | 154–156 ⁹ |
| 8 |  |  | 130 | 94 | 161–163 | 162–164 ⁹ |
| 9 |  |  | 130 | 42 | 203–205 | 205–208 ⁶⁸ |
| 10 |  |  | 130 | 51 | 244–246 | 247–250 ⁵⁷ |
| 11 |  |  | 130 | 00 | – | – |
| 12 |  |  | 130 | 00 | – | – |

Table 3. Synthesis of 1,2,4,5- tetra phenyl imidazole substituted in the presence of FeCeO_x/g-C₃N₄ nanocomposite. ^a Isolated yields.

and favor the formation of the desired product, leading to higher yields. Conversely, electron-donating groups may hinder the reaction progress, resulting in lower yields.

Optimization of the reaction parameters for the synthesis of 2,4,5-trisubstituted imidazoles

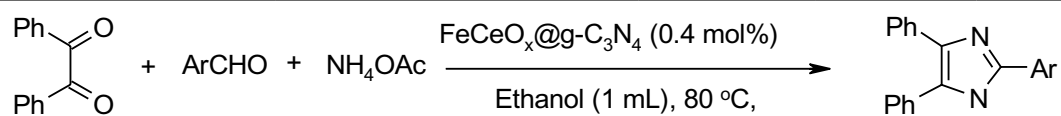
Based on our previous results, further optimization was carried out in the model reaction of benzaldehyde, benzil, and ammonium acetate. Reaction conditions were optimized by varying catalysts, solvents, and temperatures. The model reaction was initially carried out in the absence of the catalyst (Table 4, entry 1), leading to a low product yield. Various kinds of catalysts were used in this reaction (Table 4, entries 2–7), and the best result has been ascertained to $\text{FeCeO}_x/\text{g-C}_3\text{N}_4$. Finally, different amounts of $\text{FeCeO}_x/\text{g-C}_3\text{N}_4$ nanocomposite were used to determine their effects on the reaction in the presence of ethanol at 80 °C (Table 4, entries 7–9). The optimum amount of catalyst was 20 mg for the synthesis of 2,4,5-triphenyl imidazole in the reaction of benzaldehyde (0.5 mmol), benzil (0.5 mmol), and ammonium acetate (1.5 mmol) (Table 4, entry 9). The model reaction was investigated at different temperatures (Table 4, entries 8–10). As a result, the best choice was 80 °C as the optimal temperature in ethanol as a solvent for this reaction. Based on Table 4 inspection, it was observed that the optimum condition for the synthesis of 2,4,5-triphenyl imidazole was benzaldehyde (0.5 mmol), benzil (0.5 mmol), ammonium acetate (1.5 mmol), and 20 mg of $\text{FeCeO}_x/\text{g-C}_3\text{N}_4$ nanocomposite as a catalyst in ethanol as a solvent in 80 °C.

After determining the optimal conditions in the model reaction, various aldehydes, including aromatic, heteroaromatic, and aliphatic types, were employed to synthesize different imidazoles under the optimized conditions. The results of these reactions are presented in Table 5. In general, benzaldehydes with various substituents, whether electron-withdrawing or electron-donating groups, exhibited good reactivity and provided the corresponding 2,4,5-trisubstituted imidazoles in moderate to good yields. This suggests that a wide range of benzaldehydes can be utilized as substrates in this reaction, allowing for the incorporation of diverse substituents into the imidazole framework. The yields of the reactions were further influenced by the nature of the substituents on the benzaldehyde. When benzaldehydes with strong electron-withdrawing substituents like NO_2 were used (Table 5, entries 7 and 9), the reaction yields were increased. This indicates that electron-withdrawing groups enhance the reactivity and favor the formation of the desired products, leading to higher yields. However, when aliphatic aldehydes were employed (Table 5, entry 11), the yields of the corresponding imidazoles were low. This suggests that aliphatic aldehydes may not be as suitable for this transformation under the given optimized conditions.

TON = 9.4×10^{-6} and TOF $1.3 \times 10^{-9} \text{ s}^{-1}$

| Entry | Catalysts | Amount of catalyst: mg (mol) | Time (min) | Solvent | Temp. (°C) | Yield (%) ^a |
|-------|--|------------------------------|------------|---------------|------------|------------------------|
| 1 | Without catalyst | – | 220 | Ethanol | 80 | 41 |
| 2 | $\text{g-C}_3\text{N}_4$ | 20 (0.022) | 120 | Ethanol | 80 | 54 |
| 3 | $\text{SbCl}_3/\text{g-C}_3\text{N}_4$ | 20 (0.062) | 120 | Ethanol | 80 | 61 |
| 4 | $\text{CeCl}_3/\text{g-C}_3\text{N}_4$ | 20 (0.078) | 120 | Ethanol | 80 | 78 |
| 5 | $\text{FeCl}_3/\text{g-C}_3\text{N}_4$ | 20 (0.00078) | 120 | Ethanol | 80 | 63 |
| 6 | $\text{FeCl}_3/\text{CeCl}_3/\text{g-C}_3\text{N}_4$ | 20 (0.0059) | 120 | Ethanol | 80 | 87 |
| 7 | $\text{FeCeO}_x/\text{g-C}_3\text{N}_4$ | 10 (0.0023) | 120 | Ethanol | 80 | 92 |
| 8 | $\text{FeCeO}_x/\text{g-C}_3\text{N}_4$ | 20 (0.0047) | 120 | Ethanol | 25 | 82 |
| 9 | $\text{FeCeO}_x/\text{g-C}_3\text{N}_4$ | 20 (0.0047) | 120 | Ethanol | 60 | 91 |
| 10 | $\text{FeCeO}_x/\text{g-C}_3\text{N}_4$ | 20 (0.0047) | 100 | Ethanol | 80 | 98 |
| 11 | $\text{FeCeO}_x/\text{g-C}_3\text{N}_4$ | 50 | 100 | Ethanol | 80 | 98 |
| 12 | $\text{FeCeO}_x/\text{g-C}_3\text{N}_4$ | 20 (0.0047) | 120 | Water | 25 | 64 |
| 13 | $\text{FeCeO}_x/\text{g-C}_3\text{N}_4$ | 20 (0.0047) | 120 | Water | 80 | 81 |
| 14 | $\text{FeCeO}_x/\text{g-C}_3\text{N}_4$ | 20 (0.0047) | 120 | Methanol | 25 | 78 |
| 15 | $\text{FeCeO}_x/\text{g-C}_3\text{N}_4$ | 20 (0.0047) | 120 | Methanol | 80 | 90 |
| 16 | $\text{FeCeO}_x/\text{g-C}_3\text{N}_4$ | 20 (0.0047) | 120 | Acetonitrile | 25 | 68 |
| 17 | $\text{FeCeO}_x/\text{g-C}_3\text{N}_4$ | 20 (0.0047) | 120 | Acetonitrile | 80 | 82 |
| 18 | $\text{FeCeO}_x/\text{g-C}_3\text{N}_4$ | 20 (0.0047) | 120 | Ethyl acetate | 25 | 66 |
| 19 | $\text{FeCeO}_x/\text{g-C}_3\text{N}_4$ | 20 (0.0047) | 120 | Ethyl acetate | 80 | 84 |

Table 4. The effect of various parameters on the synthesis of 2,4,5-triphenyl imidazole. ^a Isolated yields.



| Entry | Aldehyde | Product | Time (min.) | Yield (%) ^a | Melting point | |
|-------|----------|---------|-------------|------------------------|---------------|----------------------|
| | | | | | Found | Reported |
| 1 | | | 80 | 98, (97) ^b | 276–278 | 276–278 ² |
| 2 | | | 80 | 95 | 228–230 | 230–231 ⁷ |
| 3 | | | 80 | 96 | 272–274 | 274–276 ² |
| 4 | | | 100 | 78 | 264–266 | 266–268 ² |
| 5 | | | 90 | 94 | 262–263 | 262–264 ⁷ |
| 6 | | | 90 | 91 | 188–189 | 190–192 ⁷ |
| 7 | | | 100 | 81 | 239–240 | 240–242 ² |

Continued

| Entry | Aldehyde | Product | Time (min.) | Yield (%) ^a | Melting point | |
|-------|----------|---------|-------------|------------------------|---------------|-----------------------|
| | | | | | Found | Reported |
| 8 | | | 90 | 93 | 256–258 | 258–260 ⁷ |
| 9 | | | 100 | 72 | 229–230 | 228–230 ¹¹ |
| 10 | | | 90 | 92 | 261–263 | 262–264 ⁴⁸ |
| 11 | | | 100 | 78 | 228–230 | 225–230 ⁵⁷ |
| 11 | | | 100 | 29 | 168–170 | 169–171 ¹⁴ |

Table 5. Synthesis of 2,4,5- triphenyl imidazole substituted in the presence $\text{FeCeO}_x\text{@g-C}_3\text{N}_4$ nanocomposite. ^a isolated yields. Yields for five gram scale.

Recycle experiments

Recyclability is an important aspect of catalysts in terms of green chemistry, and experiments were conducted on a larger scale (2.5 mol) to reduce system errors and evaluate the catalyst's reusability. In this case, 100 mg of the $\text{FeCeO}_x\text{@g-C}_3\text{N}_4$ nanocomposite catalyst was used for 5 mol of starting materials. After the completion of the reaction, 10 mL of ethyl acetate was added to the reaction mixture, and the catalyst was separated from the mixture using centrifugation. The separated catalyst was then washed with ethyl acetate. The washed catalyst was successfully reused for four consecutive runs of reactions without any significant decrease in reaction yields. As shown in Fig. 8, the yields of the four runs for the synthesis of 2,4,5-trisubstituted imidazoles (red column) were 98%, 97%, 97%, and 95%. Similarly, the yields for the four runs of synthesis of 1,2,4,5-tetrasubstituted imidazoles (blue column) were 98%, 97%, 95%, and 94%, respectively. The amount of catalyst remaining after the five runs was 93 mg, indicating a minor loss of catalyst during the recycling process.

To further confirm the stability of the $\text{FeCeO}_x\text{@g-C}_3\text{N}_4$ nanocomposite, TGA analysis and FTIR spectroscopy were performed on both the fresh and recycled catalyst. The results from TGA analysis and FTIR spectra showed no appreciable changes in the chemical structure of the recycled $\text{FeCeO}_x\text{@g-C}_3\text{N}_4$ after five cycles, further indicating its stability and suitability for reuse (Supporting information).

Table 6 provides a comparison of the catalytic efficiency of different methods reported in the literature for the synthesis of tetrasubstituted imidazoles. The $\text{FeCeO}_x\text{@g-C}_3\text{N}_4$ catalyst is specifically evaluated in the model reaction and compared to other catalysts used in similar reactions. The $\text{FeCeO}_x\text{@g-C}_3\text{N}_4$ catalyst demonstrated excellent activity and outperformed the other catalysts in the set (58–60,66,68).

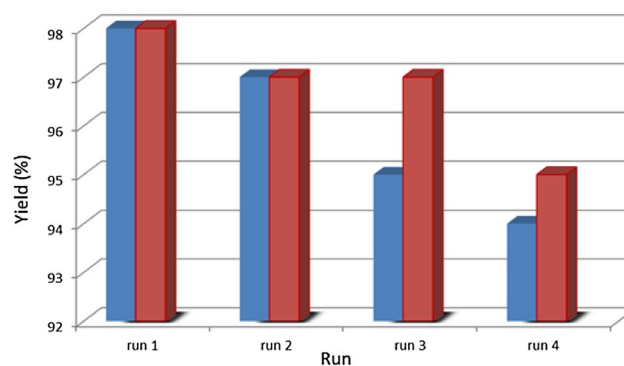


Figure 8. Recyclability of $\text{FeCeO}_x\text{@g-C}_3\text{N}_4$ nanocatalyst in the preparation of tri substituted imidazole (red chart) and four substituted imidazole (blue chart).

| Entry | Catalyst | Solvent | Time (h) | Yield (%) | Temp. (°C) | Reusability | References |
|-------|---|---------|----------|-----------|------------|-------------|------------|
| 1 | B(OH ₃) | MeOH | 8 | 60–97 | 60 | No | 61 |
| 2 | HPVAC-20 | IL | 1 | 86–94 | 120 | Yes | 1 |
| 3 | SLS | Water | 2 | 80–90 | 80 | No | 62 |
| 4 | Dendrimer-PWA ^b | – | 1 | 82–96 | 90 | Yes | 63 |
| 5 | MCS-GT@Co(II) | EtOH | 5 | 67–99 | Reflux | Yes | 13 |
| 6 | H-BEA(15) | – | 1 | 81–99 | 100 | Yes | 7 |
| 7 | [bmim] ₃ [GdCl ₆] | IL | 2.5 | 88–95 | 120 | Yes | 64 |
| 8 | DBSA | Water | 4 | 73–86 | Reflux | No | 65 |
| 9 | Cu@imine/Fe ₃ O ₄ | – | 0.5 | 93–98 | 80 | Yes | 67 |
| 10 | FeCeO _x @g-C ₃ N ₄ | Ethanol | 2 | 81–98 | 60 | Yes | This work |

Table 6. Comparison of the catalytic efficiency of various catalyst in the literature.

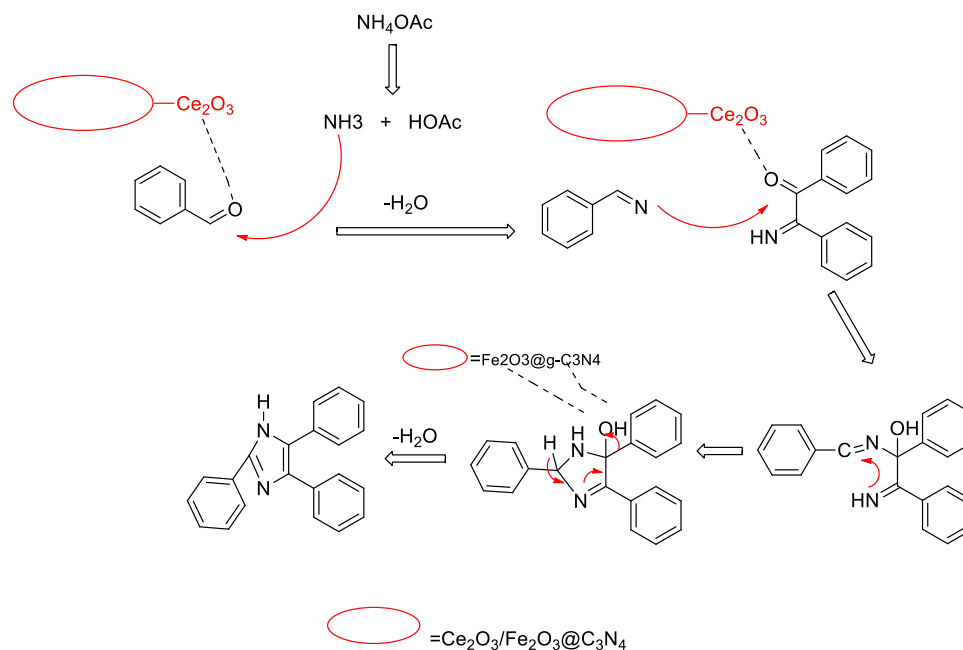


Figure 9. Proposed mechanism of the synthesis of trisubstituted imidazoles.

A reasonable mechanism for the synthesis of trisubstituted imidazoles using the $\text{FeCeO}_x@g\text{-C}_3\text{N}_4$ nanocomposite as a catalyst is illustrated in Fig. 9.

The mechanism can be described as follows: The reaction begins with the condensation of an aldehyde and ammonium acetate in the presence of $\text{FeCeO}_x@g\text{-C}_3\text{N}_4$ catalyst. The catalyst facilitates the formation of an imine intermediate through the nucleophilic addition of the amine group of ammonium acetate to the carbonyl group of the aldehyde. The imine intermediate then undergoes a subsequent reaction with a benzyl compound. This reaction can involve the nucleophilic attack of the nitrogen atom in the imine intermediate on the electrophilic carbon atom of the benzyl compound. Following the nucleophilic attack, a rearrangement occurs, leading to the formation of a trisubstituted imidazole. This rearrangement step involves the migration of substituents within the intermediate, resulting in the desired trisubstituted imidazole product. It is important to note that cerium oxide (CeO_2) plays a crucial role in this transformation. The presence of cerium oxide in the $\text{FeCeO}_x@g\text{-C}_3\text{N}_4$ nanocomposite likely enhances the catalytic activity and stability of the catalyst. Additionally, the $\text{FeCeO}_x@g\text{-C}_3\text{N}_4$ nanocomposite exhibits a synergistic effect, leading to increased yields of the trisubstituted imidazole product (Fig. 9).

Conclusion

In summary, the $\text{FeCeO}_x@g\text{-C}_3\text{N}_4$ nanocomposite is synthesized by calcinating melamine and immobilizing Ce(III) and Fe(III) on graphitic carbon nitride ($g\text{-C}_3\text{N}_4$). This iron-based nanocomposite, in combination with cerium functionality and the good surface area of $g\text{-C}_3\text{N}_4$, shows great potential for one-pot preparations of imidazole derivatives, resulting in good to excellent yields within short reaction times. The heterogeneous catalyst is easily separated and can be reused in subsequent reactions. This nanocomposite offers several advantages as a catalyst for imidazole synthesis, including its efficient performance, easy separation, and recyclability.

Experimental

Materials and chemicals

Melting points were measured in open capillaries with the Buchi 535 melting-point apparatus. The reactions were monitored by thin-layer chromatography (TLC) with UV light as detecting agents. EDS spectra and Scanning Electron Microscope (SEM) images were prepared via the TESCAN Vega3 Model. Powder X-ray diffraction (XRD) analyses were given in a Bruker AXS-D₈ Advance diffractometer. Fourier transfer infrared spectroscopy (FT-IR) in Shimadzu IR-460. ¹H NMR spectra were recorded on a 500 MHz spectrometer and ¹³C NMR spectra on a 125 MHz NMR spectrometer, respectively, using CDCl_3 or $\text{DMSO}(D_6)$ as a solvent; chemical shifts have been expressed in ppm downfield from TMS.

Catalyst preparation

Synthesis of $g\text{-C}_3\text{N}_4$

According to our previous paper, the bulk $g\text{-C}_3\text{N}_4$ was synthesized by directly heating melamine in air methods^{43,44}. 10 g of melamine powder was placed in a covered 50 mL alumina crucible and then heated in a muffle furnace at a ramp rate of 5 °C/min and kept for three h at 550 °C in air. After cooling to room temperature, a light yellow powder was collected and stored for further use. The $g\text{-C}_3\text{N}_4$ nanosheets are prepared by thermal exfoliation in the air. In detail, 2 g of bulk $g\text{-C}_3\text{N}_4$ was put into an uncovered crucible for heat treatment at 550 °C for 3 h to obtain white powder.

Synthesis of $\text{FeCeO}_x@g\text{-C}_3\text{N}_4$ nanocomposite

At first, the $g\text{-C}_3\text{N}_4$ (400 mg), which was synthesized in the previous step, was placed in a 200 mL Erlenmeyer and then dispersed in 100 mL of methanol/water (1:1) using sonication for 10 min at room temperature. Then, 40 mg CeCl_3 and 40 mg FeCl_3 was dispersed in methanol, and 20 mL NaOH (2 M) was added to the mixture and sonicated for 10 min. Henceforward, the mixture was stirred for 5 h at 60 °C, and the mixture was filtered and washed with 10 mL of methanol and dried overnight at 60 °C under vacuum to obtain $\text{FeCeO}_x@g\text{-C}_3\text{N}_4$.

General procedure for synthesizing 1,2,4,5-tetraphenyl imidazole

To a mixture of aniline (0.5 mmol), benzaldehyde (0.5 mmol), benzil (0.5 mmol) and ammonium acetate (0.5 mmol), $\text{FeCeO}_x@g\text{-C}_3\text{N}_4$ (20 mg) as catalyst and ethanol (1 mL) as a solvent were added in a 5 mL round-bottomed flask respectively. The reaction mixture was stirred with a stirrer at 60 °C for 2 h, and TLC monitored the progress of the reaction. After the reaction was completed, 20 mL of ethyl acetate was added, the catalyst was removed by centrifuge, and the catalyst was washed with ethyl acetate and reused for the subsequent reactions. The organic residue was recrystallized to obtain 1,2,4,5-tetraphenyl imidazole and derivatives as pure products.

General procedure for the synthesis of 2,4,5-triphenyl imidazole

A mixture of benzaldehyde (0.5 mmol), benzil (0.5 mmol), ammonium acetate (1.5 mmol), $\text{FeCeO}_x@g\text{-C}_3\text{N}_4$ (20 mg) as a catalyst, and ethanol (1 mL) as a solvent were placed in a 5 mL round-bottomed flask, respectively. The reaction mixture was stirred with a stirrer at 80 °C for 100 min, and TLC monitored the progress of the reaction. After the reaction was completed, 10 mL of ethyl acetate was added, and the catalyst was removed by centrifuge. Then, the catalyst was washed with hot ethanol and ethyl acetate and reused for the subsequent reactions. The ethanolic residue was recrystallized to obtain 2,4,5-triphenyl imidazole and derivatives as pure products.

Data availability

The data that support the findings of this study are available on request from the corresponding author.

References

- Karthikeyan, C., Padmavathi, V. & Suresh, R. Imidazole derivatives as potential therapeutic agents: A comprehensive review. *Eur. J. Med. Chem.* **160**, 331–353. <https://doi.org/10.1016/j.ejmech.2018.10.056> (2018).
- Shalmali, S., Rahmat Ali, M. D. & Bawa, S. Imidazole: An essential edifice for the identification of new lead compounds and drug development. *Mini Rev. Med. Chem.* **18**, 142–163. <https://doi.org/10.2174/1389557517666170228113656> (2018).
- Zhang, Z. H., Zhang, X. N., Mo, L. P., Lia, Y. X. & Ma, F. P. Catalyst-free synthesis of quinazoline derivatives using low melting sugar-urea-salt mixture as a solvent. *Green Chem.* **14**, 1502–1506. <https://doi.org/10.1039/C2GC35258C> (2012).
- Kumar, D. *et al.* Selectivity control during the solid supported protic acids catalysed synthesis of 1,2-disubstituted benzimidazoles and mechanistic insight to rationalize selectivity. *RSC Adv.* **3**, 91–98. <https://doi.org/10.1039/C2RA21994H> (2013).
- Zhang, Z. H., Yin, L. & Wang, Y. M. An expeditious synthesis of benzimidazole derivatives catalyzed by Lewis acids. *Catal. Commun.* **8**, 1126–1132. <https://doi.org/10.1016/j.catcom.2006.10.022> (2007).
- Jadhavar, P. S. *et al.* Synthesis, biological evaluation and structure-activity relationship of 2-styrylquinazolones as anti-tubercular agents. *Bioorg. Med. Chem. Lett.* **26**, 2663–2669. <https://doi.org/10.1016/j.bmcl.2016.04.012> (2016).
- Gabla, J. J., Mistry, S. R. & Maheria, K. C. An efficient green protocol for the synthesis of tetra-substituted imidazoles catalyzed by zeolite BEA: Effect of surface acidity and polarity of zeolite. *Catal. Sci. Technol.* **7**, 5154–5156. <https://doi.org/10.1039/C7CY01398A> (2017).
- Liu, C. *et al.* Selective synthesis of oxazoles and pyrazines from α -bromo-1-phenylethanone using a by-product-promoted strategy. *Tetrahedron* **74**, 7351–7357. <https://doi.org/10.1016/j.tet.2018.10.071> (2018).
- Kumari, M., Jain, Y., Yadav, P., Laddha, H. & Gupta, R. Synthesis of Fe_3O_4 -DOPA-Cu magnetically separable nanocatalyst: A versatile and robust catalyst for an array of sustainable multicomponent reactions under microwave irradiation. *Catal. Lett.* **149**, 2180–2194. <https://doi.org/10.1007/s10562-019-02794-8> (2019).
- Huang, W. *et al.* Synthesis of multisubstituted pyrroles from enolizable aldehydes and primary amines promoted by iodine. *J. Org. Chem.* **84**, 5655–5666. <https://doi.org/10.1021/acs.joc.9b00596> (2019).
- Ahoovie, T. S., Azizi, N., Yavari, I. & Hashemi, M. M. Magnetically separable and recyclable g-C₃N₄ nanocomposite catalyzed one-pot synthesis of substituted imidazoles. *J. Iran. Chem. Soc.* **15**, 855–862. <https://doi.org/10.1007/s13738-017-1284-9> (2018).
- Bhosale, S. V. *et al.* One-pot synthesis of 2,4,5-tri substituted imidazoles using $\text{MoO}_3/\text{SiO}_2$, an efficient and recyclable catalyst. *Synth. Commun.* **41**, 762–769. <https://doi.org/10.1080/00397911003644415> (2011).
- Aziizi, N., Manochehri, Z., Nahayi, A. & Torkashvand, S. A facile one-pot synthesis of tetrasubstituted imidazoles catalyzed by eutectic mixture stabilized ferrofluid. *J. Mol. Liq.* **196**, 153–158. <https://doi.org/10.1016/j.molliq.2014.03.013> (2014).
- Siddiqui, S. A. *et al.* Room temperature ionic liquid promoted improved and rapid synthesis of 2,4,5-triaryl imidazoles from aryl aldehydes and 1,2-diketones or α -hydroxyketone. *Tetrahedron* **61**, 3539–3546. <https://doi.org/10.1016/j.tet.2005.01.116> (2005).
- Shabalin, D. A. & Camp, J. E. Recent advances in the synthesis of imidazoles. *Org. Biomol. Chem.* **18**, 3950–3964. <https://doi.org/10.1039/d0ob00350f> (2020).
- Zhu, A., Qiao, L., Tana, P. & Pan, J. Interfaces of graphitic carbon nitride-based composite photocatalysts. *Inorg. Chem. Front.* **7**, 4754–4793. <https://doi.org/10.1039/D0QI01026J> (2020).
- Kong, Y., Lv, C., Zhang, C. & Chen, G. Cyano group modified g-C₃N₄: Molten salt method achievement and promoted photocatalytic nitrogen fixation activity. *Appl. Surf. Sci.* **515**, 146009. <https://doi.org/10.1016/j.apsusc.2020.146009> (2020).
- Zheng, Y., Liu, J., Liang, J., Jaroniec, M. & Qiao, S. Z. Graphitic carbon nitride materials: Controllable synthesis and applications in fuel cells and photocatalysis. *Energy Environ. Sci.* **5**, 6717–6731 (2012).
- Thomas, A. *et al.* Graphitic carbon nitride materials: Variation of structure and morphology and their use as metal-free catalysts. *J. Mater. Chem.* **18**, 4893–4908. <https://doi.org/10.1039/B800274F> (2008).
- Dong, G., Zhang, Y., Pan, Q. & Qiu, J. A. fantastic graphitic carbon nitride (g-C₃N₄) material: Electronic structure, photocatalytic and photoelectronic properties. *J. Photochem. Photobiol. C.* **20**, 33–50 (2014).
- Yang, S. *et al.* Design, synthesis and application of new iron-based cockscomb-like photocatalyst for high effectively degrading water contaminant under sunlight. *Appl. Surf. Sci.* **525**, 146559. <https://doi.org/10.1016/j.apsusc.2020.146559> (2020).
- Zhao, Z., Sun, Y. & Dong, F. Graphitic carbon nitride based nanocomposites: A review. *Nanoscale* **7**, 15–37. <https://doi.org/10.1039/C4NR03008G> (2015).
- Acharya, R. & Parida, A. review on $\text{TiO}_2/\text{g-C}_3\text{N}_4$ visible-light- responsive photocatalysts for sustainable energy generation and environmental remediation. *J. Environ. Chem. Eng.* **8**, 103896. <https://doi.org/10.1016/j.jece.2020.103896> (2020).
- Raha, S. & Ahmaruzzaman, M. Enhanced performance of a novel superparamagnetic g-C₃N₄/NiO/ZnO/Fe₃O₄ nanohybrid photocatalyst for removal of esomeprazole: Effects of reaction parameters, co-existing substances and water matrices. *Chem. Eng. J.* **395**, 124969. <https://doi.org/10.1016/j.cej.2020.124969> (2020).
- Chen, L. *et al.* Single-sites Rh-phosphide modified carbon nitride photocatalyst for boosting hydrogen evolution under visible light. *Appl. Catal. B Environ.* **273**, 119050. <https://doi.org/10.1016/j.apcatb.2020.119117> (2020).
- Niu, P., Zhang, L., Liu, G. & Cheng, H.-M. Graphene-like carbon nitride nanosheets for improved photocatalytic activities. *Adv. Funct. Mater.* **22**, 4763–4770. <https://doi.org/10.1002/adfm.201200922> (2012).
- Zhang, P. *et al.* Visible-light-induced metal-free allylic oxidation utilizing a coupled photocatalytic system of g-C₃N₄ and N-hydroxy compounds. *Adv. Synth. Catal.* **353**, 1447–1451. <https://doi.org/10.1002/adsc.201100175> (2011).
- Xiang, Q., Yu, J. & Jaroniec, M. Preparation and enhanced visible-light photocatalytic H₂-production activity of graphene/C₃N₄ composites. *J. Phys. Chem. C* **115**(15), 7355–7363. <https://doi.org/10.1021/jp200953k> (2011).
- Sheng, Y. *et al.* Enhanced organic pollutant photodegradation via adsorption/photocatalysis synergy using a 3D g-C₃N₄/TiO₂ free-separation photocatalyst. *Chem. Eng. J.* **370**, 287–294. <https://doi.org/10.1016/j.cej.2019.03.197> (2019).
- Chand, H., Kumar, A., Goswami, S. & Krishnan, V. Comparison of catalytic activity of graphitic carbon nitrides derived from different precursors for carbon dioxide conversion. *Fuel* **357**, 129757. <https://doi.org/10.1016/j.fuel.2023.129757> (2024).
- Moya, A. & Youk, J. H. Mechanochemical synthesis of graphitic carbon nitride/graphene oxide nanocomposites for dye sorption. *Dyes Pigments* **220**, 111725. <https://doi.org/10.1016/j.dyepig.2023.111725> (2023).
- Smykalová, A., Foniok, K., Cvejn, D., Górecki, K. M. & Peraus, P. The role of guanidine hydrochloride in graphitic carbon nitride synthesis. *Sci. Rep.* **11**, 21600. <https://doi.org/10.1038/s41598-021-01009-8> (2021).
- Hojamberdiev, M. *et al.* Synergistic effect of g-C₃N₄, Ni(OH)₂ and halloysite in nanocomposite photocatalyst on efficient photocatalytic hydrogen generation. *Renew. Energy* **138**, 434–444. <https://doi.org/10.1016/j.renene.2019.01.103> (2019).
- Wei, X. N. & Wang, H. L. Preparation of magnetic g-C₃N₄/Fe₃O₄/TiO₂ photocatalyst for visible light photocatalytic application. *J. Alloy Compd.* **763**, 844–856. <https://doi.org/10.1016/j.jallcom.2018.06.031> (2018).
- He, H. *et al.* Distinctive ternary CdS/Ni₂P/g-C₃N₄ composite for overall water splitting: Ni₂P accelerating separation of photocarriers. *Appl. Catal. B Environ.* **249**, 246–256 (2019).
- Li, Y. *et al.* Construction of g-C₃N₄/PDI@MOF heterojunctions for the highly efficient visible light-driven degradation of pharmaceutical and phenolic micropollutants. *Appl. Catal. B Environ.* **250**, 150–162. <https://doi.org/10.1016/j.apcatb.2019.03.024> (2019).

37. Zhang, R. *et al.* Atomically dispersed Mo atoms on amorphous g-C₃N₄ promotes visible-light absorption and charge carriers transfer. *Appl. Catal. B Environ.* **250**, 273–279. <https://doi.org/10.1016/j.apcatb.2019.03.025> (2019).
38. Xue, S. *et al.* Direct Z-Scheme charge transfer in heterostructured MoO₃/g-C₃N₄ photocatalysts and the generation of active radicals in photocatalytic dye degradations. *Environ. Pollut.* **250**, 338–345. <https://doi.org/10.1016/j.envpol.2019.04.010> (2019).
39. Liu, C., Wang, J., Yang, S., Li, X. & Lin, X. Ag₃PO₄ nanocrystals and g-C₃N₄ quantum dots decorated Ag₂WO₄ nanorods: ternary nanoheterostructures for photocatalytic degradation of organic contaminants in water. *RSC Adv.* **9**, 8065–8072. <https://doi.org/10.1039/C8RA09815H> (2019).
40. Di, J. Q. *et al.* Copper anchored on phosphorus g-C₃N₄ as a highly efficient photocatalyst for the synthesis of N-arylpiperidin-2-amines. *Green Chem.* **23**, 1041–1049. <https://doi.org/10.1039/D0GC03400B> (2021).
41. Song, H. Y. *et al.* Semi-heterogeneous g-C₃N₄/NaI dual catalytic C–C bond formation under visible light. *Green Chem.* **25**, 3292–3296. <https://doi.org/10.1039/D2GC04843D> (2023).
42. Verma, S. K. *et al.* Heterogeneous graphitic carbon nitrides in visible-light-initiated organic transformations. *Green Chem.* **24**, 438–479. <https://doi.org/10.1039/D1GC03490A> (2022).
43. Wang, X. *et al.* A metal-free polymeric photocatalyst for hydrogen production from water under visible light. *Nat. Mater.* **8**, 76–80. <https://doi.org/10.1038/nmat2317> (2009).
44. Wen, D. *et al.* Synergistically boosted photocatalytic production of hydrogen peroxide via protonation and oxygen doping on graphitic carbon nitride. *Nano Energy* **117**, 108917. <https://doi.org/10.1016/j.nanoen.2023.108917> (2023).
45. Chen, M. N., Mo, L. P., Cui, Z. S. & Zhang, Z. H. Magnetic nanocatalysts: Synthesis and application in multicomponent reactions. *Curr. Opin. Green Sustain. Chem.* **15**, 27–37. <https://doi.org/10.1016/j.cogsc.2018.08.009> (2019).
46. Laurent, S. *et al.* Magnetic iron oxide nanoparticles: Synthesis, stabilization, vectorization, physicochemical characterizations and biological applications. *Chem. Rev.* **108**, 2064–2110. <https://doi.org/10.1021/cr068445e> (2008).
47. Rai, P. & Gupta, D. Magnetic nanoparticles as green catalysts in organic synthesis—A review. *Synth. Commun.* **51**, 3059–3083. <https://doi.org/10.1080/00397911.2021.1968910> (2021).
48. Zhang, M., Liu, Y. H., Shang, Z. R., Hu, H. C. & Zhang, Z. H. Supported molybdenum on graphene oxide/Fe₃O₄: An efficient, magnetically separable catalyst for one-pot construction of spiro-oxindole dihydropyridines in deep eutectic solvent under microwave irradiation. *Catal. Commun.* **88**, 39–44. <https://doi.org/10.1016/j.catcom.2016.09.028> (2017).
49. Lu, A.-H., Salabas, E. L. & Schüth, F. Magnetic nanoparticles: Synthesis, protection, functionalization, and application. *Angew. Chem. Int. Ed.* **46**, 1222–1244. <https://doi.org/10.1002/anie.20060> (2007).
50. Gao, G., Di, J. Q., Zhang, H. Y., Mo, L. P. & Zhang, Z. H. A magnetic metal organic framework material as a highly efficient and recyclable catalyst for synthesis of cyclohexenone derivatives. *J. Catal.* **387**, 39–46. <https://doi.org/10.1016/j.jcat.2020.04.013> (2020).
51. Zhang, H. Y. *et al.* A magnetic metal–organic framework as a highly active heterogeneous catalyst for one-pot synthesis of 2-substituted alkyl and aryl(indolyl)kajic acid derivative. *N. J. Chem.* **41**, 7108–7115. <https://doi.org/10.1039/C7NJ01592E> (2017).
52. Pankhurst, Q. A., Connolly, J., Jones, S. K. & Dobson, J. Applications of magnetic nanoparticles in biomedicine. *J. Phys. D Appl. Phys.* **36**, R167–R181. <https://doi.org/10.1088/0022-3727/36/13/201> (2003).
53. Sun, C., Lee, J. S. H. & Zhang, M. Magnetic nanoparticles in MR imaging and drug delivery. *Adv. Drug Deliv. Rev.* **60**, 1252–1265. <https://doi.org/10.1016/j.addr.2008.03.018> (2008).
54. Azizi, N., Ahoie, T. S., Hashemi, M. M. & Yavari, I. Magnetic graphitic carbon nitride-catalyzed highly efficient construction of functionalized 4H-pyrans. *Synlett* **29**, 645–649. <https://doi.org/10.1055/s-0036-1589145> (2018).
55. Seyyed Shahabi, S., Azizi, N. & Vatanpour, V. Tuning thin-film composite reverse osmosis membranes using deep eutectic solvents and ionic liquids toward enhanced water permeation. *J. Membr. Sci.* **610**, 118267. <https://doi.org/10.1016/j.memsci.2020.118267> (2020).
56. Azizi, N., Khajeh, M. & Alipour, M. Rapid and selective oxidation of alcohols in deep eutectic solvent. *Ind. Eng. Chem. Res.* **53**, 15561–15565. <https://doi.org/10.1021/ie502019z> (2014).
57. Kidwai, M. & Mothra, P. A one-pot synthesis of 1,2,4,5-tetraarylimidazoles using molecular iodine as an efficient catalyst. *Tetrahedron Lett.* **47**, 5029–5031. <https://doi.org/10.1016/j.tetlet.2006.05.097> (2006).
58. Haile Asressu, K., Chan, C. K. & Wang, C. C. TMSOTf-catalyzed synthesis of trisubstituted imidazoles using hexamethyldisilazane as a nitrogen source under neat and microwave irradiation conditions. *RSC Adv.* **11**, 28061–28071. <https://doi.org/10.1039/D1RA05802A> (2021).
59. Kadu, V. D., Mali, G. A., Khadul, S. P. & Kothe, G. J. Simple practical method for synthesis of trisubstituted imidazoles: An efficient copper catalyzed multicomponent reaction. *RSC Adv.* **11**, 21955–21963. <https://doi.org/10.1039/D1RA01767E> (2021).
60. Singh, H. & Rajput, J. K. Co(II) anchored glutaraldehyde crosslinked magnetic chitosan nanoparticles (MCS) for synthesis of 2,4,5-trisubstituted and 1,2,4,5-tetrasubstituted imidazoles. *Appl. Organomet. Chem.* **32**, e3989 (2018).
61. Azizi, N., Dado, N. & Amiri, A. K. Highly efficient one-pot synthesis of trisubstituted imidazoles under catalyst-free conditions. *Can. J. Chem.* **90**, 195–198. <https://doi.org/10.1139/v11-141> (2012).
62. Bansal, R., Soni, P. K. & Halve, A. K. Green synthesis of 1,2,4,5-tetrasubstituted and 2,4,5-trisubstituted imidazole derivatives involving one-pot multicomponent reaction. *J. Heterocycl. Chem.* **55**, 1308–1312 (2018).
63. Tambe, A., Gadhave, A., Pathare, A. & Shirole, G. Novel Pumice@SO₃H catalyzed efficient synthesis of 2,4,5-triarylimidazoles and acridine-1,8-diones under microwave assisted solvent-free path. *Sustain. Chem. Pharm.* **22**, 100485. <https://doi.org/10.1016/j.scp.2021.100485> (2021).
64. Akbari, A. Tri(1-butyl-3-methylimidazolium) gadolinium hexachloride, ([bmim]₃[GdCl₆]), a magnetic ionic liquid as a green salt and reusable catalyst for the synthesis of tetrasubstituted imidazoles. *Tetrahedron Lett.* **57**, 431–434. <https://doi.org/10.1016/j.tetlet.2015.12.053> (2016).
65. Das, B., Kashanna, J., Kumar, R. A. & Jangili, P. Synthesis of 2,4,5-trisubstituted and 1,2,4,5-tetrasubstituted imidazoles in water using p-dodecylbenzenesulfonic acid as catalyst. *Monatsh. Chem.* **144**, 223–226. <https://doi.org/10.1007/s00706-012-0770-0> (2013).
66. Rossi, R., Angelici, G., Casotti, G., Manzini, C. & Lessi, M. Catalytic synthesis of 1,2,4,5-tetrasubstituted 1H-imidazole derivatives: state of the art. *Adv. Synth. Catal.* **361**, 2737–2803. <https://doi.org/10.1002/adsc.201801381> (2019).
67. Thwin, M., Mahmoudi, B., Ivaschuk, O. A. & Yousif, Q. A. An efficient and recyclable nanocatalyst for the green and rapid synthesis of biologically active polysubstituted pyrroles and 1,2,4,5-tetrasubstituted imidazole derivatives. *RSC Adv.* **9**, 15966–15975. <https://doi.org/10.1039/C9RA02325A> (2019).
68. Naidoo, S. & Jeena, V. Molecular iodine/DMSO mediated oxidation of internal alkynes and primary alcohols using a one-pot, two step approach towards 2,4,5-trisubstituted imidazoles: Substrate scope and mechanistic studies. *Tetrahedron* **76**, 131028. <https://doi.org/10.1016/j.tet.2020.131028> (2020).

Acknowledgements

This work was supported by the research facilities of the Chemistry and Chemical Engineering Research Center of Iran.

Author contributions

M.E. performed material preparation, data collection, and analysis. M.S. wrote the first draft of the manuscript. N.A. was supervised and wrote—the review and editing. All authors read and approved the final manuscript.

Competing interests

The authors declare no competing interests.

Additional information

Supplementary Information The online version contains supplementary material available at <https://doi.org/10.1038/s41598-023-44747-7>.

Correspondence and requests for materials should be addressed to N.A.

Reprints and permissions information is available at www.nature.com/reprints.

Publisher's note Springer Nature remains neutral with regard to jurisdictional claims in published maps and institutional affiliations.



Open Access This article is licensed under a Creative Commons Attribution 4.0 International License, which permits use, sharing, adaptation, distribution and reproduction in any medium or format, as long as you give appropriate credit to the original author(s) and the source, provide a link to the Creative Commons licence, and indicate if changes were made. The images or other third party material in this article are included in the article's Creative Commons licence, unless indicated otherwise in a credit line to the material. If material is not included in the article's Creative Commons licence and your intended use is not permitted by statutory regulation or exceeds the permitted use, you will need to obtain permission directly from the copyright holder. To view a copy of this licence, visit <http://creativecommons.org/licenses/by/4.0/>.

© The Author(s) 2023